CATRINA (2024), 32 (1):97-113

Assessment of Salen Schiff Base as a Corrosion Inhibitor on Low-Carbon Steel in HCl Media: Practical and Computational Studies

Amal R. El Tohamy[1*], Medhat M. Kamel[1], Ahmed Aboelmagd[1], Salah. M. Rashwan[1], Abd El-Aziz El-Sayed Fouda[2], Mohamed K. Awad[3], Faten. M. Atlam[3]

[1]Department of Chemistry, Faculty of Science, Suez Canal University, Ismailia, 41522, Egypt
[2]Department of Chemistry, Faculty of Science, Mansoura University, Mansoura, 35516, Egypt
[3]Department of Chemistry, Faculty of Science, Tanta University, Tanta, 31527, Egypt

Received: October 5, 2023; Accepted: June 26, 2024

ABSTRACT

Corrosion poses a significant challenge to the longevity and performance of metallic materials, particularly low-carbon steel, in acidic environments such as hydrochloric acid (HCl). The use of corrosion inhibitors is a widely adopted strategy to mitigate this issue, enhancing the durability and service life of metal components. Thus, the objective of this work is to study the inhibition performance of N,N′-bis(salicylidene)ethylene-1,2-diamine Schiff base (Salen SB) for low-carbon steel (CS) in 0.5 M HCl. The study was conducted using weight loss (WL), electrochemical impedance spectroscopy (EIS), and potentiodynamic polarization (PP) techniques. The Salen SB was prepared and characterized using ^{1}H NMR and FTIR techniques. The efficiency of inhibition increased with an increase in Salen SB concentration. At a concentration of 300 ppm, the inhibitor exhibited the highest efficiency of 75.4% at 298 K. However, this efficiency decreased to 69.5% when the temperature was raised from 298 K to 333 K. The tested compound reduced both the double-layer capacitance (C_{dl}) and the corrosion current (I_{corr}), indicating the formation of a protective layer on the carbon steel (CS) surface. Additionally, the inhibitor demonstrated a mixed-type behavior, which was consistent with the Langmuir adsorption isotherm. It was revealed through scanning electron microscopy (SEM) and energy dispersive X-ray (EDX) investigations that the presence of the Salen SB facilitates the formation and adsorption of a stationary film on the CS surface. To further elucidate the interactions between Salen SB molecules and CS, density functional theory (DFT) and Monte Carlo (MC) simulations were employed. The quantum properties of Salen SB demonstrate its efficacy as an inhibitor. The findings from the DFT and MC simulations indicated that Salen SB interacts with the CS surface via the lone pair of electrons from the heteroatoms, as well as the π-electrons of the benzene ring. The calculated binding energy for this interaction was -160.150 kJ/mol.

Keywords: Carbon steel; Electrochemical Impedance Spectroscopy (EIS); Green corrosion inhibition; HCl medium; Inhibition efficiency; Material durability; Salen Schiff base.

INTRODUCTION

Corrosion causes the deterioration of metal properties by means of chemical or electrochemical reactions. CS is frequently utilized in many industrial and engineering fields because of its good mechanical characteristics, ease of accessibility, and economical effectiveness in comparison with various materials (Padash *et al.*, 2019); although there are many methods for maintaining CS surfaces, the most efficient method is to use inhibitors (Hassannejad and Nouri, 2018; Nabatipour *et al.*, 2020; Saha *et al.*, 2016; Srivastava *et al.*, 2017). The use of corrosion inhibitors is a widely adopted strategy to mitigate this issue, enhancing the durability and service life of metal components.

There are two main classes of corrosion inhibitors: inorganic and organic. Inorganic inhibitors, such as NO_2^-, NO_3^-, CrO_4^{2-}, $Cr_2O_7^{2-}$, and PO_4^{3-}, have been successful in controlling corrosion, but their adverse effects on the environment continue to be an important disadvantage. These substances, particularly chromates, have poor biological compatibility and are environmentally harmful (Olasunkanmi *et al.*, 2020). The most effective compounds, however, are organic inhibitors because they have one or more polar groups in addition to π-electrons (El Faydy *et al.*, 2018). By adhering to the metal's surface and creating a barrier film, they successfully suppress corrosion (Al-Baghdadi *et al.*, 2021; Bahaa El-Dien *et al.*, 2019). Schiff bases are among these organic compounds that have strong potential to inhibit the corrosion of CS under a variety of conditions, particularly with sulfuric and hydrochloric acids (Abdallah *et al.*, 2019; Al-Najjar and Al-Baitai, 2022; Alwan, 2018; Chen *et al.*, 2021; Hashemi *et al.*, 2021; Jamil *et al.*, 2018; Nazir et *al.*, 2020; Wang, 2021; Zhang *et al.*, 2019). Schiff bases, particularly those derived from Salen ligands, have garnered attention due to their effectiveness and eco-friendliness. A few researchers reported that the unoccupied π* orbitals in Schiff base molecules are responsible for the effectiveness of inhibition. The bond between inhibitor and metal is stabilized as the π* orbitals facilitate the back donation of electrons from the metal to the inhibitor. In addition to being used in industry as corrosion inhibitors, Schiff bases and their compounds have significant applications as antibiotics, antioxidants, and anti-inflammatory drugs (Al-Amiery *et al.*, 2020; Jaafar and Saeed, 2020; Saha *et al.*, 2021).

* *Corresponding author e-mail: amal_refaat@science.suez.edu.eg*

Natash Mary *et al*. (2022) investigated the effectiveness of two Schiff bases derived from triazoles:

4-[(furan-2-ylmethylidene)amino]-5-methyl-4H-1, 2, 4-triazole-3-thiol (FAMTT) and 4-[(4-chlorobenzylidene)amino]-5-methyl-4H-1,2,4-triazole-3-thiol (CAMTT). These compounds were tested for their ability to inhibit the corrosion of steel in a mixture of hydrochloric acid (HCl) and sulfuric acid (H_2SO_4) at a 2:1 ratio. The results indicated that as the temperature and concentration of the Schiff bases increased, the inhibitory effectiveness of both derivatives also rose. DFT calculations and experimental findings were correlated, and both showed that FAMTT is more efficient than CAMTT.

The Isatin Schiff base 2-(2-oxoindolin-3-ylidene) hydrazinecarbothioamide (OHB) was prepared by Al-Amiery *et al.,* (2022). They used electrochemical and gravimetric techniques to examine the corrosion resistance of mild steel specimens in 1.0 M HCl. Their research findings demonstrated the mixed-type and significant corrosion inhibition of OHB. The efficiency of inhibition increased as the temperature rose. Hegazy *et al.* (2021) have tested the azomethine compound (6E, 7E)-N1, N 6-bis (1-methylpyrrolidin-2-ylidene) hexane-1, 6-diamine as a CS corrosion inhibitor in a 0.5 M H_2SO_4 solution. They asserted that increasing the quantity of the synthetic inhibitor in the corrosive media enhances the inhibition efficiency.

In a 0.1 M HCl solution, Al-Najjar and Al-Baitai (2022) created and characterized a novel imidazole derivative, (N, N'E, N'E)-N, N'-(thiophene-2,5-diylbis(methanylylidene)) bis(1Hbenzo[d]imidazol-2-amine). Their results demonstrated that the inhibition efficiency rose with increasing compound dose; however, it decreased with rising temperature. At 0.5 mM of the manufactured inhibitor, 96% inhibition efficiency was the highest.

Kumari and Lavanya (2021) investigated the impact of the Schiff base N'-[4-(dimethylamino) benzylidene]-4-hydroxybenzohydrazide on the prevention of the dissolution of mild steel in HCl solution. The potency of the synthetic inhibitor to attach to mild steel was confirmed based on its kinetic and thermodynamic characteristics. According to the experimental findings, the chemical compounds under investigation appear to have strong inhibition properties.

The aim of this work is to synthesize a Salen Schiff base, characterize it, and examine its ability to inhibit CS corrosion in a solution of 0.5 M HCl. The corrosion experiments were completed using WL, EIS, and PP techniques. EDX and SEM were used to examine the CS surface. A variety of adsorption isotherms were used to understand how Salen Schiff base exists at the CS surface. In addition, some thermodynamic and activation characteristics have been estimated. Furthermore, DFT and MC simulations were performed to explain how Salen Schiff base molecules interacted with the CS surface.

MATERIALS AND METHODS

The CS utilized in the corrosion experiments has the subsequent composition (wt. %):0.201 C, 0.602 Mn, 0.041 P, 0.0031 Si, 0.05 S, and the rest is Fe. The composition was determined using EDX analysis. Proton nuclear magnetic resonance (^{1}HNMR) spectra were collected on a Vario Germany 300 MHz spectrometer in dimethyl sulphoxide (DMSO) as the solvent. Fourier-transform infrared spectroscopy (FTIR) spectra have been captured on a Bruker Alpha 11 Germany infrared spectrometer. The electrochemical measurements were performed on OrigaLys Potentiostat - OGS 100.

Synthesis of N, N′-bis(salicylidene)butylene-1,4-diamine (SB)

Salicylaldehyde (4 mmol) and 1,2-diaminorthane (2 mmol) were refluxed together for 4 hours in ethanol to create Salen SB (Ab *et al.,* 2015). Yellow crystals having a melting point of 126–129 °C were obtained. The yield was 95.27%. Fig. (1) shows the chemical composition of the Salen SB.

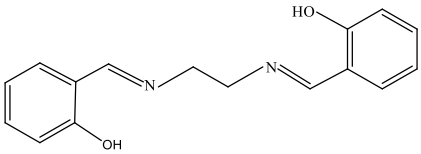

Figure (1): N, N′- bis (salicylidene) ethylene-1, 2-diamine (Salen SB). Mol. Formula: $C_{18}H_{24}O_2N_2$; Mol. Wt.: 384.56.

WL method

WL was established on CS in 0.5 M HCl medium without and with various doses (50–300 ppm) of Salen SB for 3 h within the temperature range of 298-333 K. The acidic solution was applied to a surface area of 9 cm^2 of CS. The weights of the polished, cleaned, and dried specimens were measured before they were submerged in the acidic solution. All samples were placed in a pickling solution ($SnCl_2$ and $SbCl_3$ in 1:1 HCl) for 2 min to eliminate the corrosion products. The sample is then cleaned with 5% $NaHCO_3$ before being dried, weighed, and finally washed with distilled water (AATIAOUI *et al.,* 2021). The rate of corrosion (CR) was computed using the following equation:

$$CR = \frac{W1 - W2}{At}$$

Where, W_1 and W_2 are the masses of CS prior to and after submerging in the corrosion medium, respectively, A is the CS area per cm^2, and t is the submerging duration in seconds. Meanwhile, the inhibition efficiency (IE_w) was calculated using the equation:

$$IE_w = \frac{Wo - Wi}{Wo} \times 100$$

$$\theta = \frac{Wo - Wi}{Wo}$$

Where, W_o and W_i are the WL devoid of and with the inhibitor, respectively. θ is the surface coverage of CS.

Electrochemical techniques

The corrosion behavior of CS was studied using PP and EIS techniques. A cell containing a Pt counter electrode, a CS rod as the working electrode (WE), and Ag/AgCl as a reference electrode was utilized for the study. The WE with a surface area of 1 cm^2 was polis-

hed with materials of varying abrasiveness and cleaned with ethanol and double-distilled H_2O prior to usage. To achieve the greatest stability, the electrode was eventually inserted into the testing medium at the open-circuit potential (OCP) for 30 mins. PP study was recorded in the potential range of -150 to -650 mV against Ag/AgCl with a scan rate of 1 mV s^{-1}. The method of Stern-Geary was used to determine the corrosion current for every concentration of the Salen SB and the blank solution. All investigations were performed at 25°C and performed 3 times to ensure precision. Using AC pulses at OCP with $5X10^{-3}$ V^3 peak to peak amplitude, the EIS was carried out in the frequency range of 100 kHz to $5X10^{-4}$ Hz. Both the Bode and Nyquist types of the EIS graphs were drawn. PP and EIS were established via the biological instrument OrigaLys Potentiostat (OGS 100) and the EC-LAB program. For data visualization, graphing, and fitting, Origin 2021 and Microsoft Office 2016 were utilized.

Surface examination

CS specimens were submerged in 0.5 M HCl media in the nonexistence and existence of 300 ppm of Salen SB for 72 hrs. Then, they were washed with distilled water, dried, and tested by SEM on a BED-C 10 kV, Jeol equipped with an EDX instrument to exa-mine the surface topography and the composition of the adsorbed coating.

Computational studies

Computational studies were used to link the quantum chemical characteristics with the claimed inhibition activity of the tested compound and to explain the mechanism of adsorption. Quantum operators were computed using DFT/6-31+G (d) and MC simulations.

RESULTS

Validation of the synthesized Salen SB's structure

^{1}HNMR study

The ^{1}HNMR spectrum of Salen SB showed a singlet peak appearing at 3.90 ppm that corresponds to the 4 protons of the two -CH_2N groups. In addition, the ^{1}HNMR spectrum demonstrated the characteristic signals of the 8 aromatic protons of the two salicylidene rings as several signals between 6.84-7.42 ppm and a singlet peak at 8.56 ppm for the two protons of the two -CH=N groups in addition to a broad signal for the two OH protons between 13.30-13.5 ppm. The ^{1}HNMR spectrum of Salen SB is displayed in Figure (2).

FTIR study

IR patterns demonstrate peaks at 1283.91 cm^{-1} that correspond to (C-O), 1498.06 cm^{-1} corresponding to (C=C), 1622.09 cm^{-1} (C=N) and peak appears in the region of 3740.31 to 3864.56 cm^{-1} corresponding to (OH), Figure (3).

WL measurements

The inhibition impact of the Salen SB was evaluated at various concentrations in a 0.5 M of HCl solution. The table (1) presents the corrosion rate (CR), contact angle (θ) and inhibition efficiency (IE_w). The corrosion rate decreases as the concentration of the substance increases. Starting from a blank value of 1.80 ± 0.3 mg cm^{-2} s^{-1}, after which it declines steadily to 0.44 ± 0.3 mg cm^{-2} s^{-1} at 300 ppm. Meanwhile, the contact angle increased as the concentration Salen SB increased which enhance the inhibition of CR. These results clearly indicate an improvement in surface hydrophobicity, which can be linked to better protection against corrosion as the surface becomes less wettable by the corrosive medium. Consequently, the inhibition efficiency showed a clear upward trend with increasing concentrations of the corrosion inhibitor (Table 1).

The general patterns in the results show a clear correlation between the substance's concentration and corrosion-inhibiting efficacy. Greater hydrophobic qualities, improved inhibitory efficiency, and decreased corrosion rates are all correlated with higher concentrations. These results suggest that improving this substance's concentration may result in more successful corrosion control techniques in appropriate applications. Future researches are in need to examine the inhibitory effect's long-term stability as well as its usefulness in actual corrosion situations.

The impact of temperature

Data presented in Table (2) on corrosion rates (CR) across different concentrations and temperatures, provides valuable insights into the behavior of metal corrosion in relation to varying conditions, in which the corrosion rates at lower temperatures (298 K to 313 K) noticeably decrease as the inhibitor concentration rises (from 50 ppm to 300 ppm). However, at higher temperatures (323 K and 333 K), where corrosion rates start to converge, these inhibitors lose their effectiveness. Meanwhile, data showed that the greatest rate of corrosion was observed at higher temperatures even when inhibitors are not present. These results indicate that higher temperatures may enhance the corrosive effects under the same condition. The observed trend suggests that higher tempera-tures generally improve reaction kinetics, most likely as a result of increased molecular mobility and reactant

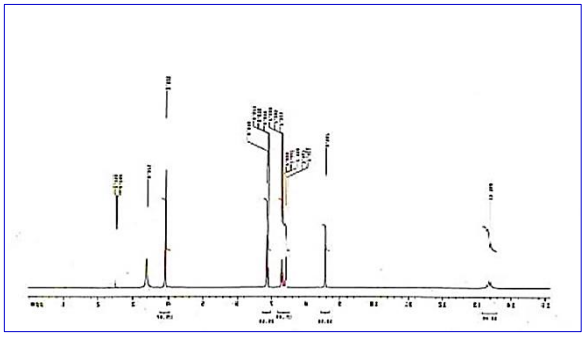

Figure (2): ^{1}HNMR spectrum of Salen SB.

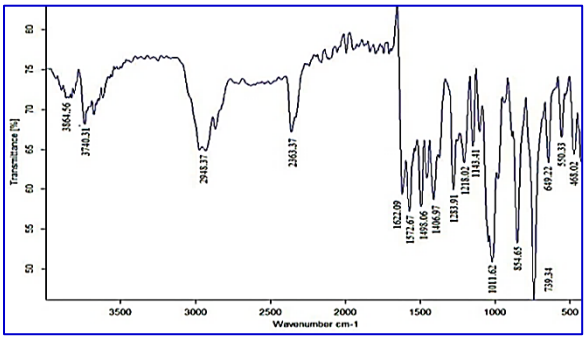

Figure (3): IR spectra of Salen SB.

collision frequency. At lower concentrations, where temperatures greatly increase the CR values, the response is most noticeable. This observed result indicates that, generally, higher temperatures enhance reaction kinetics, likely due to higher molecular motion and collision frequency among reactants. The response is most pronounced at lower concentrations, where temperatures significantly elevate the CR values. Meanwhile, the decline in reaction rates at higher concentrations may suggest a threshold concentration beyond which additional substrate does not facilitate an increase in the rate, potentially due to saturation effects or other kinetic phenomena. Therefore, further study is in need to determine this threshold concentration under tested conditions.

Thermodynamic and activation parameters

Understanding of the behavior of an inhibitor during the adsorption process relies on thermodynamic factors. For the corrosion process of CS in a 0.5 M of HCl solution, the activation parameters, such as activation energy (E_a^*), enthalpy change (ΔH_a^*), and entropy change (ΔS_a^*) have been estimated. The transition-state and Arrhenius plots for the Salen SB compound (lnk_{corr} (corrosion factor) vs. T^{-1} and ln k_{corr}/T vs. T^{-1}, respectively) are displayed in Figure (4).

In the given system, the activation energy (E_a^*) steadily rises with concentration from 23.32 kJ mol^{-1} (blank) to 27.45 kJ mol^{-1} at 300 ppm, as shown in Table (4), which also offers data on other thermodynamic parameters and their correlation with concentration (ppm). This suggests that greater concentrations might strengthen the chemical reaction barrier, either as a result of steric interference or enhanced molecule interactions. Additionally, the enthalpy change (ΔH_a^*) gradually increases from 20.64 kJ mol^{-1} in the blank to 24.57 kJ mol^{-1} at 300 ppm. According to this pattern, the heat content of the reaction may be rising as the concentration does, most likely due to stronger reactant interactions. The entropy shift ($-\Delta S_a^*$) appears relatively stable across the concentrations, with values fluctuating slightly around 245 J K^{-1} mol^{-1}. A stable entropic change suggests a constant energy distribution or reaction pathway and suggests that concentration variations may not have a substantial impact on the system's disorder (Table 4).

In general, higher concentrations may result in more complicated or stable chemical intermediates that need more energy to activate, as seen by the steady increase in both E_a^* and ΔH_a^* with concentration. However, the relative constant $-\Delta S_a^*$ indicates that the degree of disorder associated with the reaction is constant at all concentrations. These outputs are confirmed by the presence of a strong linear relationship between concentration and the corresponding thermodynamic parameters.

Adsorption isotherm

The surface coverage (θ) and inhibitor concentration (C_{inh}) are used to verify the specific details of Salen SB adsorption at the CS surface. Various types of isotherms were examined, such as Langmuir, Freund-lich, and Temkin. The Salen SB adsorption is consis-tent with Langmuir 's model. The fitted data is represented in Figure (5). The results collected from the isotherm are displayed in Table (5).

Electrochemical measurements

PP study

Figure (6) shows how the Salen SB affected the V-I graph of CS in 0.5 M HCl. Potentiody-namic polarization parameters of CS in 0.5 M HCl without and with various concentrations of Salen SB compound at 25 °C are shown in Table (6).

Table (1): Effect of Salen Schiff Base concentration on weight loss (WL) of carbon steel in 0.5 M HCl at 25 °C.

Conc. (ppm)	Measured parameters		
	CR (mg. cm^{-2}. s^{-1}) × 10^{-4}	θ	IE_w
Blank	1.80 ± 0.3	-	-
50	0.93 ± 0.2	0.480	48.0
100	0.72 ± 0.1	0.600	60.0
150	0.61 ± 0.1	0.657	65.7
200	0.56 ± 0.2	0.695	69.5
250	0.51 ± 0.2	0.714	71.4
300	0.44 ± 0.3	0.754	75.4

Table (2): Effect of temperature on corrosion rate of carbon steel in 0.5 M HCl at 25 °C at different Salen SB concentrations.

Conc. (ppm)	CR (mg.cm^{-2}. s^{-1}) × 10^{-4} Temperature (in Kelvin†)			
	298	313	323	333
Blank	1.80 ± 0.30	3.0 ± 0.3	3.5 ± 0.5	5.0 ± 0.2
50	0.93 ± 0.20	1.5 ± 0.2	1.8 ± 0.3	2.7 ± 0.4
100	0.72 ± 0.10	1.2 ± 0.4	1.5 ± 0.1	2.2 ± 0.1
150	0.61 ± 0.50	1.1 ± 0.5	1.3 ± 0.4	1.9 ± 0.3
200	0.56 ± 0.40	1.0 ± 0.4	1.2 ± 0.3	1.8 ± 0.2
250	0.51 ± 0.20	0.9 ± 0.1	1.1 ± 0.1	1.6 ± 0.5
300	0.44 ± 0.60	0.8 ± 0.2	0.9 ± 0.2	1.5 ± 0.6

†Temp. from Kelvin to Celsius scales: C=K-273.15.

Table (3): Effect of temperature on contact angle (θ) and inhibition efficiency (IE_w) of Salen SB at different concentrations on carbon steel placed in 0.5 M HCl.

Conc. (ppm)	Temperature (in Kelvin†)							
	298		313		323		333	
	θ	IE_w	θ	IE_w	θ	IE_w	θ	IE_w
Blank	-	-	-	-	-	-	-	-
50	0.480	48.00	0.486	48.6	0.479	47.9	0.460	46.0
100	0.600	60.00	0.580	58.0	0.569	56.9	0.551	55.1
150	0.657	65.70	0.636	63.6	0.622	62.2	0.616	61.6
200	0.690	69.50	0.650	65.0	0.642	64.2	0.630	63.0
250	0.710	71.40	0.700	0.1	0.686	68.6	0.665	66.5
300	0.750	75.40	0.733	73.3	0.718	71.8	0.695	69.5

†Temp. from Kelvin to Celsius scales: C=K-273.15.

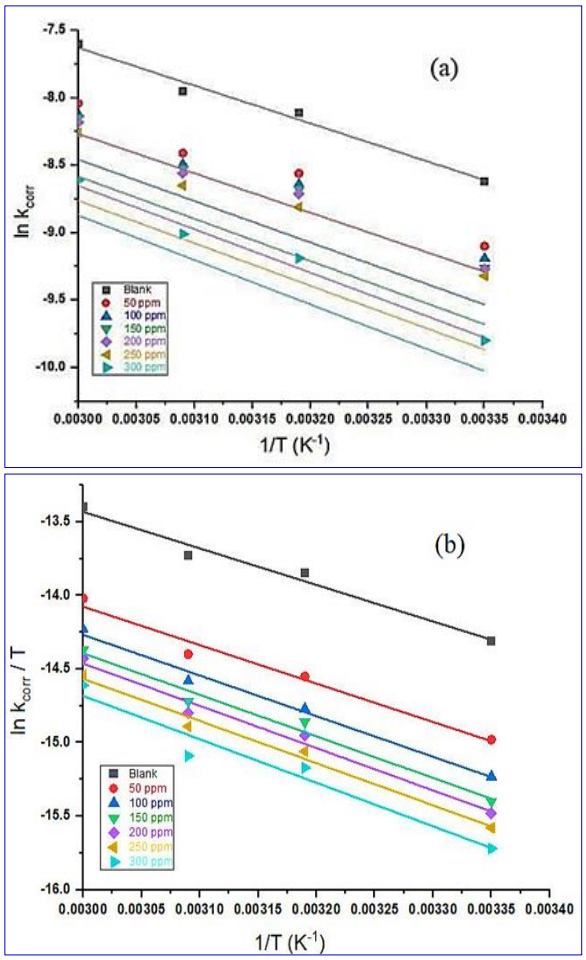

Figure (4): Arrhenius plots (a), and transition-state plots (b) for the corrosion of CS in 0.5 M of HCl without and with different concentrations of Salen SB.

Table (4): Effect of concentration on activation energy, enthalpy, and entropy changes in corrosion Inhibition by Salen SB of carbon steel in 0.5 M HCl.

Conc. ppm	E_a^* kJ mol^{-1}	ΔH_a^* kJ mol^{-1}	$-\Delta S_a^*$ J K^{-1} mol^{-1}	R^2 (Regression coefficient)
Blank	23.32	20.64	247.25	0.984
50	24.33	21.73	249.33	0.979
100	25.57	22.97	247.17	0.990
150	26.08	23.48	246.67	0.983
200	26.78	23.9	246.01	0.985
250	27.07	23.92	245.92	0.989
300	27.45	24.57	245.84	0.983

Table (5): Effect of temperature on adsorption parameters for Salen SB on carbon steel in 0.5 M HCl: Equilibrium constant (K_{ads}) and standard free energy (ΔG^o_{ads}).

Temp (K)†	Slope	Intercept	K_{ads} (mol^{-1})	$-\Delta G^o_{ads}$ (kJ mol^{-1})	R^2
298	1.18	47.97	2084.63	28.88	0.998
313	1.22	48.40	2066.11	30.31	0.995
323	1.25	48.80	2049.18	31.26	0.996
333	1.29	49.24	2030.86	32.20	0.997

†Temp. from Kelvin to Celsius scales: C=K-273.15

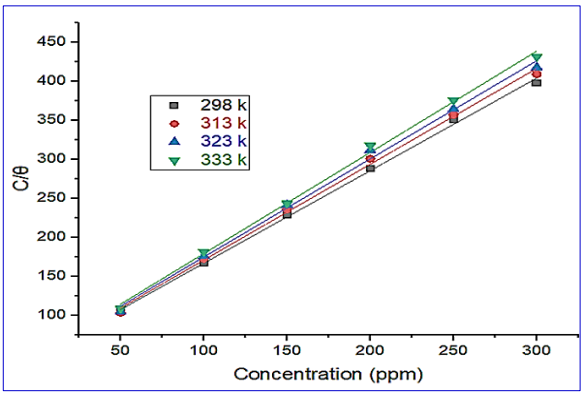

Figure (5): Langmuir adsorption isotherms for CS in 0.5 M HCl in the absence and presence of the Salen SB compound at different temperatures

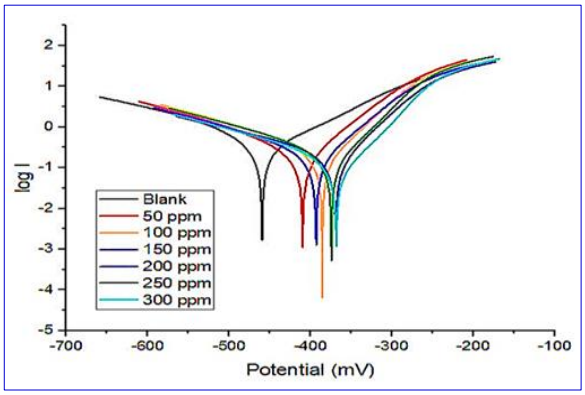

Figure (6): Tafel plots for CS in 0.5 M HCl in the absence and presence of different concentrations of Salen SB compound at 25 °C.

In table (6), the electrochemical behavior recorded that as the concentration of the inhibitor increases from the blank to 300 ppm, there is a noticeable tendency of decreasing I_{corr} values, indicating that the inhibitor effectively reduces corrosion rates at higher concentrations. This is critical as it suggests that the protective effect against corrosion is highly dependent on inhibitor concentration. In addition, the inhibition efficiency (IE_p) also recorded similar pattern in which a consistent increase with higher concentrations of the inhibitor, reaching 77.8% at 300 ppm, was documented. This signifies that not only does the decrease in I_{corr} confirm the efficiency of the inhibitor, but it also highlights its potential application in practical corrosion control scenarios.

EIS measurements

EIS studies were performed to clarify the corrosion process and describe the inhibitory mechanism. Figure (7) displays the Nyquist and Bode diagrams of CS devoid of and with various doses of Salen SB. In this Nyquist plot, the curves represent impedance data collected at varying concentrations (from 50 ppm to 300 ppm) of an additive in an electrochemical system, along with a blank (control) sample with no additive. Each curve corresponds to a specific concentration. The graph displays a semicircular trend, which is indicative of the system's charge-transfer resistance. The semicircle's size typically increases when the concentration is added. This implies that increased concentrations may have an impact on the

electrochemical characteristics, most likely raising the barrier to charge transfer. The impedance response is strongly influenced by additive concentration, as evidenced by the biggest semicircle seen in the 300 ppm concentration and the smallest in the blank sample.

For the graph (7b), it illustrates how log impedance (log[Z]) varies with log frequency for various concentrations (ppm), which is typical for impedance behavior in materials as frequency increases. In addition, as the log frequency increases (towards the right side of the graph), the impedance values across all concentrations converge towards similar values. This suggests that at higher frequencies, the influence of concentration on impedance becomes minimal.

The electrical equivalent circuit shown in Figure (7c) was utilized to analyze the impedance data that was acquired, which might be used for impedance spectroscopy analysis of materials or electrochemical cells. The circuit contains two resistors (R_s and R1), two capacitors (C_1 and C_2), and a Warburg element (represented by W).

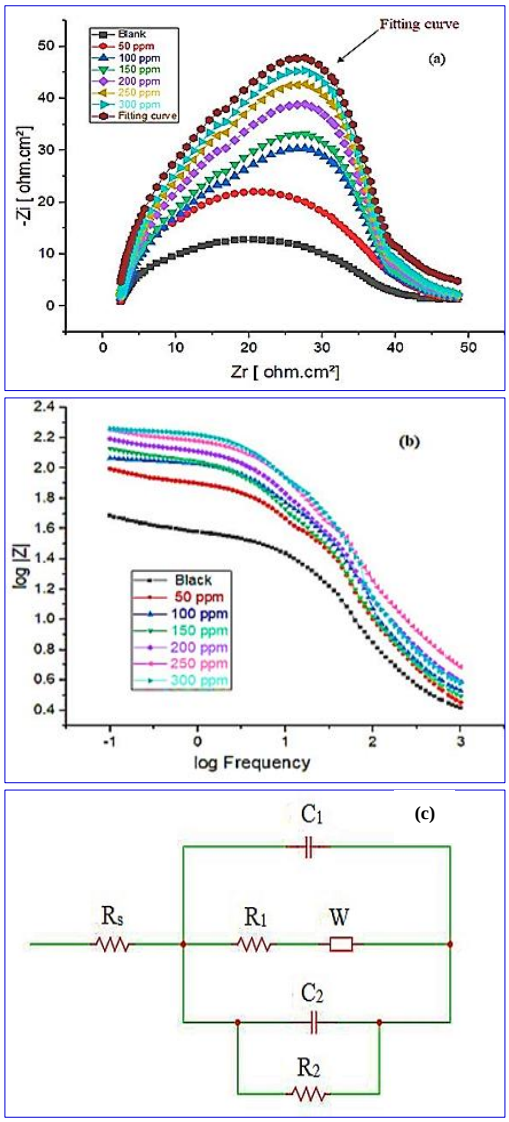

Figure (7): Nyquist (a) and Bode (b) Plots with equivalent circuit model (c) showing the effect of SB concentration on impedance and phase angle used to fit experimental EIS data.

Table (7), represent the EIS data of CS in 0.5 M HCl in which the provided data reflect an analysis of the impact of varying concentrations (ppm) on several electrical properties, including resistance (R1 and R2 in Ω cm²), Warburg impedance (W in $\Omega/s^{1/2}$), capacitance (C1 and C2 in μF), a dimensionless parameter (θ), and the percentage inhibition efficiency (%IE). For resistance, as the concentration increases from the blank sample to 300 ppm, both R1 and R2 show an upward trend. This suggests that higher concentrations may lead to increased resistance, possibly due to increased ionic interactions or a thicker layer of the substance reducing ionic mobility. Meanwhile, the Warburg impedance also increases with concentration and shows a clear relationship where W rises from a hypothetical negative value at blank to 116.64 ($\Omega/s^{½}$) at 300 ppm. This relates to the diffusion of ions; higher resistance typically means more difficulty in ion movement, correlating spontaneously with the rising concentration.

The percentage IE increases steadily with concentration, rising from 74.4 ± 0.1 at 300 ppm to no inhibition in the blank. This implies that improved performance or efficacy of the process being suppressed or aided is correlated with higher concentrations. The gradual increases in inhibition efficiency show that the concentration has a direct impact on the system's efficacy (Table 7).

Morphology and structure of the CS surface

SEM inspection

The SEM micrographs of the polished CS sheet (a), after exposure to 0.5 M HCl at ambient temperature for 72 hrs (b), and after exposure to blank solution + 300 ppm of Salen SB at ambient temperature for 72 hrs (c), are displayed in Figure (8, left panel).

EDX inspection

To explore the chemical structure of the CS surface in 0.5 M HCl, the EDX analyses of CS samples exposed to HCl solution with Salen SB verses to blank, were carried out (Figure 9).

Quantum chemical calculations

DFT results

To investigate the features of the interaction between the CS surface and the Salen SB adsorption sites, a DFT study was conducted. The quantum chemical parameters have a relation to the measured SB inhibitory efficiency. Figure (8, right panel) shows the ideal SB structures, including the HOMO and LUMO molecular orbitals that are highest occupied and lowest unoccupied, respectively.

Table (8) lists the quantum parameters that may affect the way Salen SB interacts with CS. The Table reports the electronic parameters for the energy gap (ΔE), ionization potential (I), electron affinity (A), chemical potential (μ) electronegativity (χ), global hardness (η), softness (σ), electrophilicity index (ω), nucleophilicity (ε), and a proportion of electron transfer (ΔN_{max}). The aforementioned parameters are calculated according to the following equations:

$$\Delta E = E_{\mathrm{LUMO}} - E_{\mathrm{HOMO}}$$

$$I = -E_{\mathrm{HOMO}}$$

$$A = -E_{\mathrm{LUMO}}$$

$$\mu = -\chi$$

$$\mu = \frac{(E_{\mathrm{HOMO}} + E_{\mathrm{LUMO}})}{2}$$

$$\eta = \frac{(E_{\mathrm{LUMO}} - E_{\mathrm{HOMO}})}{2}$$

$$\sigma = {}^{1}/_{\eta}$$

$$\Delta N_{\max} = \frac{-\mu}{\eta}$$

$$\omega = \frac{\mu^2}{2\eta}$$

$$\varepsilon = {}^{1}/_{\omega}$$

Where, I is the ionization energy; $E_{\ \mathrm{LUMO}}$ is the Lowest unoccupied molecular orbital; μ, denotes the chemical potential, and χ represents the electron-egativity of the molecule; HOMO, is the highest occupied molecular orbital; η, is often referred to as the energy gap or band gap; σ is the inverse of the energy gap (η); ΔN_max, is the maximum number of electrons that can be accepted by a molecule/system and ω, represents some form of energy or work associated with charge transfer.

MC simulation

Simulated annealing is a tool for optimization in Monte Carlo modeling, which is based on the theory of molecular mechanics (Kirkpatrick et al., 1983). When compared to quantum mechanical simulation, MC simulation is more efficient because it runs more quickly and costs less money. The sort of adsorption is influenced by the inhibitor's chemical composition. Using MC simulations enables us to know the adsorption behavior of the CS surface and the type of contact between the Salen SB and the CS surface. The descriptors calculated, by the Monte Carlo simulation, for the adsorption of the Salen SB compound on the CS surface was illustrated in Table (9) and figure (10).

DISCUSSION

The data obtained from WL measurements clearly display that the inhibition efficiency ameliorates as the concentration of Salen SB increases, and the highest efficiency is 75.4% at 300 ppm. The surface coverage (θ) of the adsorbed Salen SB molecules increases as its concentration increases in the corrosive medium. This result reflects that the examined compound has good inhibition properties. The CS corrosion rapidly increased as the temperature increased in ether of presence

Table (6): Potentiodynamic polarization parameters of CS in 0.5 M HCl without and with various concentrations of Salen SB compound at 25 °C.

Concn. (ppm)	$-E_{corr}\times10^{-3}$ (V)	$\beta_a\times10^{-3}$ (V dec^{-1})	$-\beta_c\times10^{-3}$ (V dec^{-1})	$I_{corr}\times10^{-3}$ (A cm^{-2})	θ	IE_p
Blank	459.5	146.5	222.8	0.7032	-	-
50	409.7	84.3	189.4	0.3479	0.505	50.5 ± 0.2
100	385.6	69.1	171.9	0.2652	0.622	62.2 ± 0.1
150	369.7	66.1	209.9	0.2137	0.696	69.6 ± 0.3
200	393.2	71.6	162.4	0.2116	0.699	69.9 ± 0.4
250	374.3	60.3	149.6	0.1889	0.731	73.1 ± 0.5
300	368.2	62.5	170.2	0.1555	0.778	77.8 ± 0.1

Table 7. EIS data of CS in 0.5 M HCl in the absence and presence of different concentrations of the Salen SB at 25 °C**.**

Conc. (ppm)	R1 (Ω cm^2)	R2 (Ω cm^2)	W (Ω / s$^{1/2}$)	C1 ×10^{-6} (F)	C2 ×10^{-6} (F)	θ	%IE
Blank	22.45	16.54	-	423.45	355.45	-	-
50	56.66	23.98	33.21	365.76	323.94	0.516	51.6 ± 0.3
100	74,31	55.76	56.83	323.87	295,66	0.619	61.9 ± 0.1
150	88.65	63.19	69.96	290.78	277.31	0.650	65.0 ± 0.4
200	101.4	78,43	87.23	240.19	212.62	0.701	70.1 ± 0.2
250	122.65	91.74	101.58	201.64	171.65	0.729	72.9 ± 0.5
300	131.24	102.34	116.64	180.97	133.87	0.744	74.4 ± 0.1

Table (8): Quantum chemical parameters obtained from DFT theory for the Salen SB molecule.

Volume (cm^3 mol^{-1})	E_t (au)	TNC (e)	ω	χ (au)	μ (au)	σ (au)$^{-1}$	η (au)	DM (Debye)	ΔE (au)	LUMO (au)	HOMO (au)
228.735	-878.997	-3.587	0.101	0.134	-0.134	11.236	0.089	2.699	0.178	-0.045	-0.223

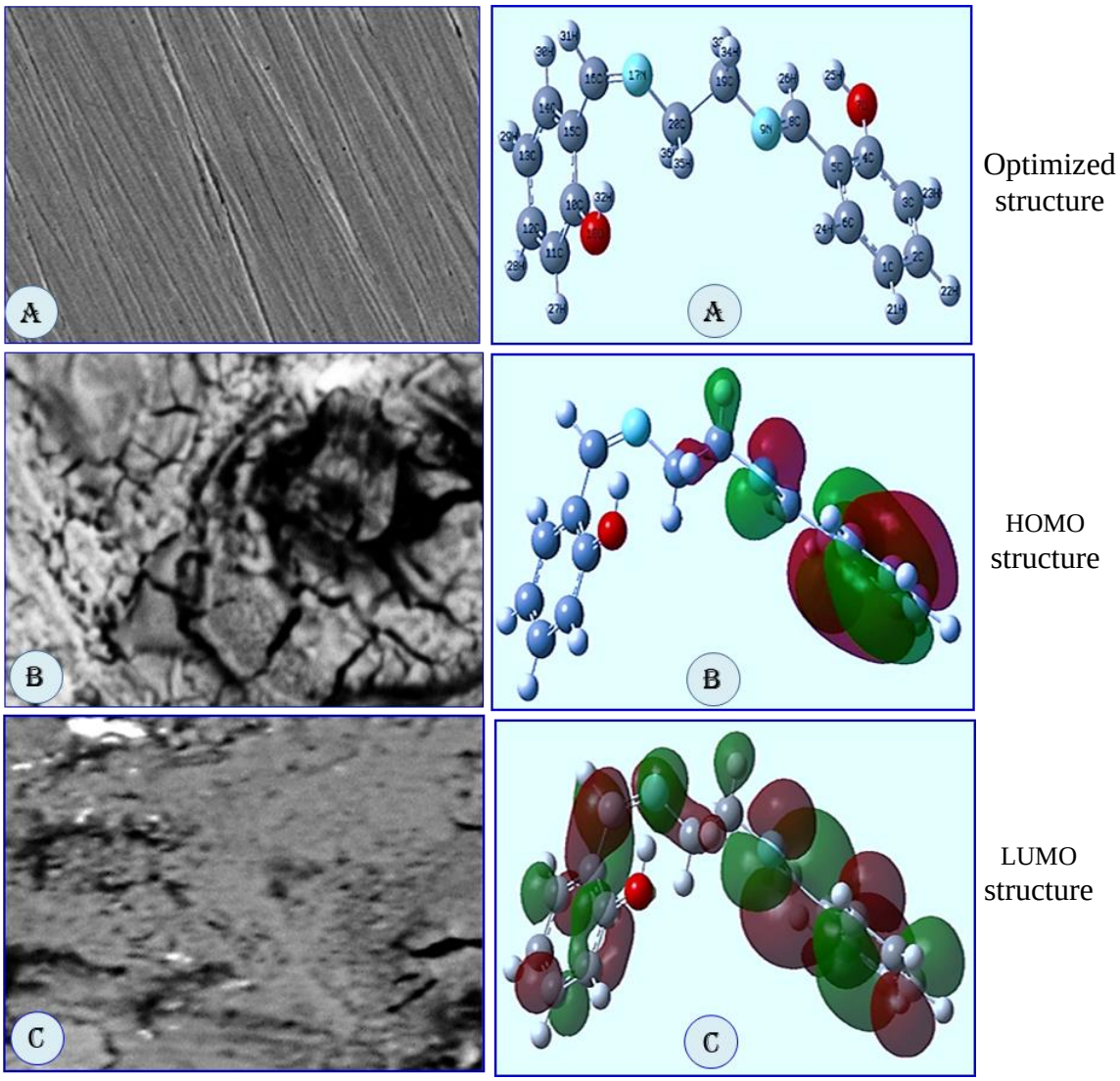

Figure (8): SEM micrographs (left panels) in comparable to molecular electronic modelling (right panels) of treated carbon steel surfaces showing morphological and chemical analysis before and after immersion in 0.5 M HCl. A, Polish carbon steel (CS); B, CS after 72 hrs immersion 0.5 M HCl; C, CS after 72 hrs immersion in 0.5 M HCl combined with the Salen SB at concentration 300 ppm.

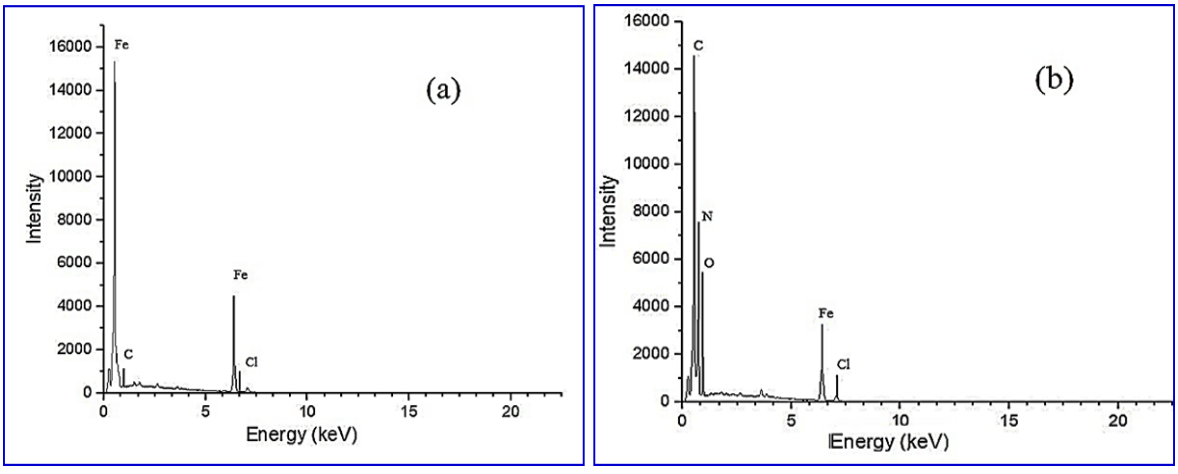

Figure (9): EDX spectra of CS specimens: (a) after immersion in 0.5 M HCl without Salen SB, and (b) with 300 ppm of the Salen SB compound.

Table (9): The descriptors calculated by the Monte Carlo simulation for the adsorption of the Salen SB compound on the CS surface.

Molecule	Total energy (kJ mol^{-1})	Adsorption energy (kJ mol^{-1})	Rigid adsorption energy(kJ mol^{-1})	Deformation energy (kJ mol^{-1})
Salen SB	-219.522	-166.15	-147.84	-18.31

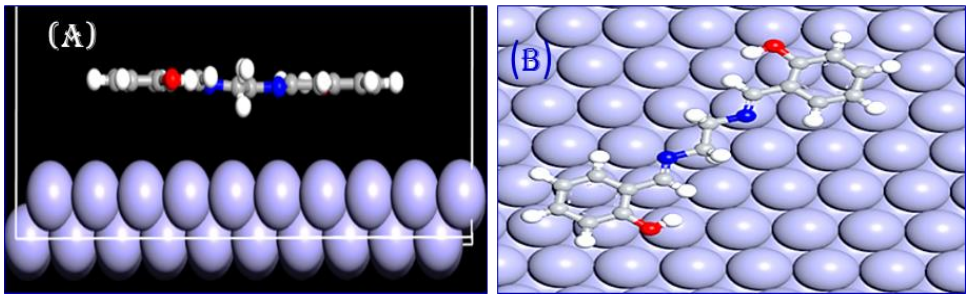

Figure (10):. Side view (A) and top view (B) for the adsorption of the Salen SB on the CS surface.

or absence of the synthesized Salen SB. This could be due to the increased impacts of rising temperature on the speed of electrochemical processes (Kamel *et al.*, 2022). With rising temperatures, the effectiveness of inhibition drops. The main factor contributing to the reduce in inhibition efficiency value at elevated temperatures may be due to the desorption of the Salen SB compound from the CS surface. Both Arrhenius and transition-state equations were employed to determine the activation parameters as follow:

$$k_{corr} = A\ exp\left(\frac{-E_a^*}{RT}\right)$$

$$ln\left(\frac{k_{corr}}{T}\right) = \left(\ln\left(\frac{k_B}{h}\right) + \left(\frac{\Delta S_a^*}{R}\right)\right) - \frac{\Delta H_a^*}{RT}$$

$$CR = k_{corr} \times i_{corr}$$

Where, k_{corr} is the corrosion factor, i_{corr} is the corrosion current, *CR* is the corrosion rate, *R* is the gas constant, k_B is the Boltzmann's constant, *T* is the Kelvin temperature, and *h* is the Planck's constant.

The Arrhenius figure, which displays a straight line with a slope of -E_a^*/R, is used to calculate the E_a^* for the corrosion process. As Salen SB retards the corrosion process, the energy of activation increases as Salen SB concentration rises. The Salen SB may attach to the CS surface, or this increase may result from a change in the potential difference at the CS-solution interface because of adsorption. Transition-state graphs display straight lines with (ln k_B/h) + (ΔS_a^*/R) as their intercepts and (-ΔH_a^*)/(R) as their slopes that utilized to determine the magnitudes of ΔS_a^* and ΔH_a^* as shown in Table (4). The positive signs of ΔH_a^* indicate that heat absorption is necessary for the formation of activated complex in the transition state. According to the negativity of ΔS_a^*, the activated complex is more ordered than the reactants. Salen SB adheres to the Langmuir adsorption isotherm. Using the following formula of Singh and Quraishi (2012), the Langmuir isotherm is determined using the following equation:

$$C_{inh} / \theta = (1 / K_{ads}) + C_{inh}$$

Where, C_{inh} is the Salen SB concentration and K_{ads} is the equilibrium constant for the adsorption process.

The CS surface's Langmuir adsorption isotherm for the Salen SB recorded the values of linear correlation coefficients, R^2, that are close to one that supports the Langmuir type of adsorption. It is worth observing that the slope of the lines is greater than 1, indicating that there are lateral interactions between adsorbed molecules (Gómez-Sánchez *et al.*, 2023). The K_{ads} were estimated using the intercepts of the straight lines. The effect of temperature also demonstrate that as temperature rises, the K_{ads} value declines (Shahabi *et al.*, 2019). In light of equation (7), the standard free energy change for adsorption ($\Delta G°_{ads}$) can be calculated as follow:

$$\Delta G°_{ads} = - RT \ln (55.5\ K_{ads})$$

Where, *R* is the gas constant, *T* is the Kelvin temperature, and 55.5 is the molar concentration of water (El-Etre *et al.*, 2015).

The negativity of $\Delta G°_{ads}$ reflects the spontaneous adsorption of the Salen SB compound onto the surface of the CS. The literature indicates that $\Delta G°_{ads}$ values can be maintained at 20 kJ mol^{-1} by electrostatic attraction between charged metals and charged molecules (physisorption). The values bigger than 40 kJ mol^{-1} suggest the occurrence of chemisorption (Al-Amiery *et al.*, 2020). The values of $\Delta G°_{ads}$ for the Salen SB range between -28.88 and -32.20 kJ mol^{-1}. This demonstrates that the examined compound slows down the dissolution of the CS by physisorption and chemisorption processes (Kamel *et al.*, 2022). Tafel plot investigates that the anodic and cathodic reactions are both delayed by the examined compound. As the Salen SB concentration increases, the corrosion current decreases. The Salen SB prevents CS from dissolution in HCl solution. The cathodic curves in Figure (6) recoded similar behaviour. This suggests that the adsorption of the examined compound at the CS surface had no or little impact on the cathode's reaction mechanism. On the contrary, the slopes of the anodic curves alter, suggesting a modified mechanism for the anodic process.

The adsorption of Salen SB at the CS surface may considerably inhibit the dissolution process. The Cl^-

species are important for the corrosion of CS in the absence of Salen SB.

$$Fe_{(s)} + Cl^- \rightarrow (FeCl)_{ads} + e$$

$$(FeCl)_{ads} \rightarrow (FeCl)^+ + e$$

$$(FeCl)^+ \rightarrow Fe^{2+} + Cl^-$$

The cathodic reactions are:

$$4H^+ + O_2 + 4e \rightarrow 2H_2O$$

$$2H^+ + 2e \rightarrow H_2$$

Olasunkanmi *et al.* (2016) found that pH values above 4 are where the effect of reduced dissolved oxygen on CS breakdown is most noticeable. H_2 evolution is thus the main cathodic process in this investigation. The values of the Tafel slopes (β_c, β_a), corrosion current (i_{corr}), and corrosion potential (E_{corr}) are shown in Table 6. The corrosion current decreases when Salen SB is present in corrosive media. It is worth noting that the change in E_{corr} values is smaller than 85 mV, proving that the tested compound belongs to mixed type. Due to the dissimilarity of the anodic and cathodic polarization lines about E_{corr}, as shown in Table 6, $\beta_c + \beta_a \neq 1$. The inhibition efficiency, IE_p, is calculated using the following equation:

$$IE_p = (1 - \frac{i_{(inh)}}{i_{(free)}}) \times 100$$

Where, $i_{(free)}$ and $i_{(inh)}$ are the corrosion currents without and with the Salen SB, respectively.

Salen SB concentration recorded an increment that principally improve the IE_p. These data support the results of the WL method (Olasunkanmi *et al.,* 2020). Electrochemical impedance experiments can often detect the formation of protective corrosion product layers or the presence of coatings on the surface of corroded metal (Kirkland *et al.,* 2012). In such cases, the EIS spectra comprise of two capacitive loops in the high- and low-frequency ranges. EIS measurements of Salen SB in 0.5 M HCl showed that Nyquist plots, depicted as semicircles. The semicircles are not perfect because of the heterogeneity of the CS electrode. The shape of Nyquist semicircles did not alter too much with the addition of Salen SB, indicating that the examined compound has no or little effect on the mechanism of the corrosion process *(*Abd El Wanees *et al.,* 2016; Kaabi *et al.,* 2021). The Nyquist plot shows more than two time constants, which indicates that the corrosion process is complex and involves multiple steps. The presence of the organic inhibitor has modified the corrosion process, but it has not eliminated it completely. The first time constant is associated with the charge transfer process at the metal/electrolyte interface. The second time constant is associated with the diffusion of ions in the electrolyte. The third time constant is associated with the adsorption of the inhibitor molecules on the metal surface. The presence of the third time constant is a good sign, as it indicates that the inhibitor molecules are adsorbing on the metal surface and forming a protective layer.

For Bode graphs, the relationship between log |Z| and log f (frequency) is directly proportional in the median frequency range. A slope's value does not attain -1. This illustrates the capacitive system's suboptimal performance at medium frequencies. To obtain the best capacitive performance at medium frequencies, it is suggested that the slope be -1 and the phase angle be -90. Solutions that are inhibited have slopes that are larger in magnitude than those that are not. This explains the suppressing properties of the investigated compound on CS dissolution. Impedance measure-ments were used to calculate the impedance param-eters, such as. C_1, C_2, R_2 (charge transfer resistance) including R_1, and W (Warburg resistance). Salen SB also recorded when concentration grows, the value of the R_2 also rises. As a result, the Salen SB's presence enhances inhibition's efficiency by reducing corrosion's rate. In addition, the values of C_1 and C_2 drop as the Salen SB concentration increases. This is mostly assigned to the fact that the Salen SB molecules are gradually replacing H_2O molecules on the CS surface. An increase in the thickness of the electrical double layer and a decrease in the dielectric constant lead to reduced capacitance values. This suggests that Salen SB molecules interact with the metal/solution interface. Adsorption occurs when Cl^- ions combine with Salen SB molecules (Hmamou *et al*., 2012).

For the suggested equivalent circuit, R_1 and C_1 represent the resistance and capacitance components of the protective corrosion layer or coating, R_2 is the charge transfer resistance, and C_2 characterizes the capacitance of the electric double layer (Man et al., 2020; Hou *et al.*, 2020). The fitting curve recoded in this study confirmed the experimental results.

The IE_i values were calculated by utilizing the following equation of Sadeek *et al.,* (2018):

$$\%\, IE_i = \left(1 - \frac{R_{ct}^o}{R_{ct}}\right) \times 100$$

Where, R_{ct} and R^o_{ct} are the charge transfer resistances in the presence and absence of the Salen SB, respectively. The subsequent equation was employed to calculate the C_{dl} as follow:

$$C_{\mathrm{dl}} = Y_{\mathrm{o}}(\omega_{\max})^{n-1}$$

Where, $\omega_{\max} = 2\pi f_{\max}$, and $f_{\max}$ is the frequency at which Z_{imag} reaches the maximum value.

The pitting impact of the Cl^- ions has extensively harmed the CS specimens exposed to the blank solution, when the Salen SB is present, it significantly improves the surface via adsorption at the CS surface. It creates a barrier film. This result is consistent with the conclusions of the WL, PP, and EIS studies and with data obtained by Bodkhe et al., (2021).

The EDX patterns of carbon steel (CS) samples in 0.5 M HCl, both with and without 300 ppm of Salen SB, recorded a reduction in corrosion of the CS. This can be attributed to the formation of a protective layer on the CS surface due to the adsorption of Salen SB, which shields it from corrosion by the aggressive HCl.

The intensity of the Fe line was reduced in the inhibited solution compared to the blank solution. The presence of O, C, and N lines indicates that the Salen SB molecules were adsorbed onto the CS surface (Chugh *et al.*, 2020). The illustration of quantum parameters demonstrates that the Salen SB's geometrical structure is not a planner. In addition, the provided structure with the lowest computed energy recoded that. The examined compound could adsorb at the CS surface via lone pairs of electrons that exist on nitrogen and oxygen atoms (Muralidharan *et al.*, n.d.).

In the light of frontier molecular orbital theory, chemical activity is produced by the relationship between the HOMO and LUMO levels of the reactants (Saadouni *et al.*, n.d.). The ability of the inhibitors to provide and receive electrons is correlated with their HOMO and LUMO energy levels, respectively. A higher HOMO energy level (E_{HOMO}) is easier to donate and a lower LUMO energy level (E_{LUMO}) is more suitable for acceptance. Also, the small value of LUMO indicates that the inhibitor has a greater ability to receive electrons. Consequently, the reduced energy band gap ($E = E_{LUMO} - E_{HOMO}$) causes a stronger interaction between the Salen SB inhibitor and the CS surface and ameliorates the inhibition efficiency (Benbouguerra *et al.*, 2018; Gao and Liang, 2007). Both the effectiveness of inhibition and the simplicity with which the inhibitor can supply electrons to the vacant d-orbital of the CS surface increase with an increasing HOMO value.

The Salen SB has a high E_{HOMO} (-0.223), low E_{LUMO} (-0.045) and a small ΔE value (0.178). So, it makes sense to assume that the Salen SB has a strong ability to adsorb at the CS surface. This expectation and the practical findings are in good agreement. The dipole moment, DM, has been utilized to describe and understand the structure (Gece and Bilgiç, 2009) DM and inhibition efficiency are closely related. The Salen SB molecule has a significant dipole moment (2.699 Debye), as shown in Table 8. Another quantum parameter that was found through computations is the molecule volume. The calculations showed that the molecular volume of the Salen SB compound, which is 228.735 cm^3 mol^{-1} is large. This large volume increases the efficiency of the inhibition as it improves the surface interaction between the Salen SB molecule and the CS surface.

Important properties that affect a molecule's stability and reactivity include its hardness and softness. In contrast to the large energy gap of a hard molecule, soft molecules have a smaller energy gap. Since soft molecules may more readily give electrons to an acceptor, they are significantly more active than hard ones. Therefore, for the easiest electron transfer, adsorption can happen where the value of σ is greatest on the molecule (Martinez, 2002). The Salen SB with a value of $\sigma = 11.236$ $(au)^{-1}$ is assumed to have a high level of inhibitory efficiency. As indicated in Table 8, the Salen SB also has a low χ and ω, but a high TNC (0.134 au, 0.101 au, and -3.587 e), respectively, in accordance with the computations. As a result, its ability to give electrons to the CS surface improves, and the inhibition efficiency increases (Kamel *et al.*, 2022). The good inhibition performance of the Salen SB compound that is supported by the quantum chemical parameters is compatible with the experimental results.

It is evident that the HOMO level of the Salen SB compound is primarily influenced by the π-bonding nature of the C-C bonds in the phenyl ring and the lone pairs of electrons on the oxygen atom in the hydroxyl (OH) group. This suggests that these sites are conducive to electrophilic attack on the carbon steel (CS) surface. Consequently, the CS surface interacts with moieties that have high HOMO density, and adsorption likely occurs through the π-electrons of the CS surface. In addition, the charge density of the LUMO level is completely localized over all Salen SB molecules. This implies that the molecule can accept electrons from CS.

The molecular electrostatic potentials (MEPs) are important as negative areas (red colour) can be act as nucleophilic centres, however, and positive parts (blue colour) as potential electrophilic centres. According to calculations, oxygen and nitrogen atoms have negative electrostatic potential, which suggests that previous atoms are the primary sites for binding with the surface of CS.

The adsorption modeling of the studied Salen SB on the CS is displayed in both top and side views in Fig. 12. The adsorption energy between the Salen SB and the CS surface is calculated by the following relation:

$$E_{ads} = E_{Fe\text{-}inh} - (E_{inh} - E_{Fe})$$

Where, E_{inh} and E_{Fe} are the total energy of both the Salen SB and CS surfaces, respectively. The MC simulation's findings showed that the adsorption energy between the Salen SB and the CS surface is -166.150 kJ mol^{-1}. This significantly negative value suggests an effective interaction between the Salen SB and CS molecules.

The mechanism of corrosion inhibition can be explained as a synthesized Salen SB molecule's has ability to act as an inhibitor depends on its chemical structure. The Salen SB molecule contains a fatty alkyl chain. This chain slows the spreading of the corrosive medium on the CS surface. According to the values of E_{corr}, β_a, and β_c (Table 6), the addition of Salen SB influences not only the reduction of oxygen gas and hydrogen ions in the cathodic area but also the oxidation of CS in the anodic area. By physisorption, the Salen SB molecules and the chloride ions in the corrosion environment create a barrier film on the CS surface, reducing the metal's contact area with the corrosive media and preventing additional CS oxidation. The chemical adsorption of the Salen SB on the metal surface is caused by the free electrons on the N and O atoms and the double bond nature of the benzene ring, according to the findings of quantum chemistry.

CONCLUSION

The Salen Schiff base compound was prepared and

characterized by ^{1}HNMR and FTIR spectroscopy. The prepared compound was assessed as a carbon steel corrosion inhibitor in 0.5 M HCl. The inhibition efficiency increased with the concentration of the Salen compound. At 300 ppm of Salen SB, the efficiency is 75.4% at room temperature. The adsorption of the Salen SB compound followed the Langmuir model and influenced the corrosion of carbon steel (CS) through both physisorption and chemisorption. Salen SB acted as a hybrid-type inhibitor. The electrochemical impedance spectroscopy (EIS) results confirmed that the presence of Salen SB in the corrosive medium reduced both the capacitance and corrosion current while increasing the charge transfer resistance, due to the formation of an adsorbed film on the CS surface. The data obtained from the various methods are strongly correlated, demonstrating the validity and reliability of the findings. The quantum characteristics of the Salen SB compound further confirm its superior inhibitory efficiency, with an adsorption energy of -166.150 kJ mol^{-1} between the Salen SB compound and the CS surface.

ACKNOWLEDGMENTS

The authors acknowledge the Chemistry Department of the Faculty of Science at Suez Canal University for their cooperation and encouragement during this work.

REFERENCES

AATIAOUI, A. EL, KOUDAD, M., CHELFI, T., ERKAC, S., AZZOUZI, M., AOUNITI, A., SAVAŞ, K., KADDOURI, M., BENCHAT, N., OUSSAID, A., 2021. Experimental and theoretical study of new Schiff bases based on imidazo(1,2-a)pyridine as corrosion inhibitor of mild steel in 1M HCl. J Mol Struct 1226. https://doi.org/10.1016/j.molstruc.2020.129372.

AB, N., SAIN, R., SHANKAR, R., GUPTA, R., PANDEY, S., SAUD, K., CHAVHAN, S.T., CHAVAN, R.P., 2015. Synthesis and characterization of novel Schiff's base Ni (II) and Fe(III) & its complexes with its anti-bacterial activity. ~ 39 ~ International Journal of Chemical Studies 3, 39–41.

ABD El WANEES, S., ALAHMDI, M.I., RASHWAN, S.M., KAMEL, M.M., ABD ELSADEK, M.G., 2016. Inhibitive effect of cetyltriphenylphosphonium bromide on C-steel corrosion in HCl solution. Int J Electrochem Sci 11, 9265–9281. https://doi.org/10.20964/2016.11.68

ABDALLAH, M., ALFAKEER, M., ALTASS, H.M., ALHARBI, A.M., ALTHAGAFI, I., HASAN, N.F., MABROUUK, E.M., 2019. The polarographic and corrosion inhibition performance of some Schiff base compounds derived from 2-amino-3-hydroxypyridine in aqueous media. Egyptian Journal of Petroleum 28, 393–399. https://doi.org/10.1016/j.ejpe.2019.09.002.

ABDEL HAMMEED, R.S., ISMAIL, E.A., Al-SHAFEY, H.I., ABBAS, M.A., 2020. Expired Indomethacin Therapeutics as Corrosion Inhibitors for Carbon Steel in 1.0 M Hydrochloric Acid Media. J Bio Tribocorros 6. https://doi.org/10.1007/s40735-020-00403-5.

Al-AMIERY, A., SALMAN, T.A., ALAZAWI, K.F., SHAKER, L.M., KADHUM, A.A.H., TAKRIFF, M.S., 2020. Quantum chemical elucidation on corrosion inhibition efficiency of Schiff base: DFT investigations supported by weight loss and SEM techniques. International Journal of Low-Carbon Technologies 15, 202–209. https://doi.org/10.1093/ijlct/ctz074

Al-AMIERY, A.A., Al-AZZAWI, W.K., ISAHAK, W.N.R.W., 2022. Isatin Schiff base is an effective corrosion inhibitor for mild steel in hydrochloric acid solution: gravimetrical, electrochemical, and computational investigation. Sci Rep 12. https://doi.org/10.1038/s41598-022-22611-4

Al-BAGHDADI, S.B., KADHIM, A., SULAIMAN, G., Al-AMIERY, A.A., ABDUL AMIR, H.K., TAKRIFF, M.S., 2021. Anticorrosion and antibacterial effects of new Schiff base derived from hydrazine, in: Journal of Physics: Conference Series. IOP Publishing Ltd. https://doi.org/10.1088/1742-6596/1795/1/012021

Al-NAJJAR, S.S., Al-BAITAI, A.Y., 2022. Synthesized of Novel Imidazole-derived Schiff Base as a Corrosion Inhibitor of Carbon St eel in Acidic Medium Supported by Electrochemical and DFT Studies. Physical Chemistry Research 10, 179–194. https://doi.org/10.22036/pcr.2021.300569.1955

ALWAN, W.M., 2018. Synthesis, Characterization and the Corrosion Inhibition Study of Two Schiff Base Ligands Derived from Urea and Thiourea and Their Complexes with Cu(II) and Hg(II) Ions, in: Journal of Physics: Conference Series. Institute of Physics Publishing. https://doi.org/10.1088/1742-6596/1003/1/012017

BAHAA El-DIEN, M.E.G., ATWA, S.T., AHMED, A.A., El-ETRE, A.Y., 2019. Synthesis and Characterization of Carbon Steel Corrosion Inhibitors Based on 4,5,6,7-tetrahydro-benzo[b]thiophene Scaffold. Protection of Metals and Physical Chemistry of Surfaces 55, 179–186. https://doi.org/10.1134/S2070205119010106

BENBOUGUERRA, K., CHAFAA, S., CHAFAI, N., MEHRI, M., MOUMENI, O., HELLAL, A., 2018. Synthesis, spectroscopic characterization and a comparative study of the corrosion inhibitive efficiency of an α-aminophosphonate and Schiff base derivatives: Experimental and theoretical investigations. J Mol Struct 1157, 165–176. https://doi.org/10.1016/j.molstruc.2017.12.049.

BODKHE RB, SHRESTHA SB, UNERTL K, FETZIK J, MCNULTY AK. Comparing the physical performance of liquid barrier films. Skin Res Technol. 2021 Sep;27(5):891-895. doi: 10.1111/srt.13038.

CHEN, S., XU, M., TANG, Q., YANG, Z., TAN, X., HE, B., HUANG, J., 2021. A Theoretical Study of

Some Schiff Bases as 304 Stainless Steel Inhibitors in HCl Solution. Int J Electrochem Sci 16, 1–11. https://doi.org/10.20964/2021.03.06

CHUGH, B., SINGH, A.K., THAKUR, S., PANI, B., LGAZ, H., CHUNG, I.M., JHA, R., EBENSO, E.E., 2020. Comparative Investigation of Corrosion-Mitigating Behavior of Thiadiazole-Derived Bis-Schiff Bases for Mild Steel in Acid Medium: Experimental, Theoretical, and Surface Study. ACS Omega 5, 13503–13520. https://doi.org/10.1021/acsomega.9b04274

EL FAYDY, M., TOUIR, R., EBN TOUHAMI, M., ZARROUK, A., JAMA, C., LAKHRISSI, B., OLASUNKANMI, L.O., EBENSO, E.E., BENTISS, F., 2018. Corrosion inhibition performance of newly synthesized 5-alkoxymethyl-8-hydroxyquinoline derivatives for carbon steel in 1 M HCl solution: Experimental, DFT and Monte Carlo simulation studies. Physical Chemistry Chemical Physics 20, 20167–20187. https://doi.org/10.1039/c8cp03226b.

EL-ETRE, A.Y., MEGAHED, H.E., REFAAT, S.M., 2015. Carbon steel corrosion in HCl in the presence of aqueous extract of Melissa Officinalis. Journal of Basic and Environmental Sciences 5, 52–62.

GAO, G., LIANG, C., 2007. Electrochemical and DFT studies of β-amino-alcohols as corrosion inhibitors for brass. Electrochim Acta 52, 4554–4559. https://doi.org/10.1016/j.electacta.2006.12.058

GECE, G., BILGIC, S., 2009. Quantum chemical study of some cyclic nitrogen compounds as corrosion inhibitors of steel in NaCl media. Corros Sci 51, 1876–1878. https://doi.org/10.1016/j.corsci.20-09.04.003.

GÓMEZ-SÁNCHEZ, GISELLE, OCTAVIO OLIVARES-XOMETL, PAULINA ARELLANES-LOZADA, NATALYA V. LIKHANOVA, IRINA V. LIJANOVA, JANETTE ARRIOLA-MOR-ALES, VÍCTOR DÍAZ-JIMÉNEZ, AND JOSUÉ LÓPEZ-RODRÍGUEZ. 2023. Temperature Effect on the Corrosion Inhibition of Carbon Steel by Polymeric Ionic Liquids in Acid Medium International Journal of Molecular Sciences 24, no. 7: 6291. https://doi.org/10.3390/ijms24076291

HASHEMI, A., MOJTABA NASR-ESFAHANI, BAKHSHESHI-RAD, H.R., 2021. Corrosion Inhibitive Property of Self-Assembled Films Formed by Schiff base Molecules on Carbon Steel Surface. Protection of Metals and Physical Chemistry of Surfaces 57, 849–857. https://doi.org/10.1134/S2070205121040080

HASSANNEJAD, H., NOURI, A., 2018. Sunflower seed hull extract as a novel green corrosion inhibitor for mild steel in HCl solution. J Mol Liq 254, 377–382. https://doi.org/10.1016/j.molliq.2-018.01.142.

HEGAZY, M.A., RASHWAN, S.M., MELEEK, S., KAMEL, M.M., 2021. Synthesis, characterization and mitigation action of innovative Schiff base on steel disintegration in sulfuric acid solution. Mater Chem Phys 267. https://doi.org/10.1016/j.match-emphys.2021.124697

HMAMOU, D. BEN, SALGHI, R., ZARROUK, A., BENALI, O., FADEL, F., ZARROUK, H., HAMMOUTI, B., 2012. Carob seed oil: an efficient inhibitor of C38 steel corrosion in hydrochloric acid. International Journal of Industrial Chemistry 3, 1–9. https://doi.org/10.1186/2228-5547-3-25.

HOU, R.Q., ZHANG, F., JIANG, P. L., DONG, S.G., LIN, C.J., 2020. Corrosion Inhibition of Pre-formed Mussel Adhesive Protein (Mefp-1) Film to Magnesium Alloy. Corros. Sci. 164, 108309.

JAAFAR, W.A., S, R.S., 2020. Synthesis, Charact-erization and Corrosion Inhibition Study of New Heterocyclic Compounds and Schiff Base with [Co (II), Ni (II), Cu (II) and Hg (II)] Complexes, Systematic Reviews in Pharmacy.

JAMIL, D.M., Al-OKBI, A.K., Al-BAGHDADI, S.B., Al-AMIERY, A.A., KADHIM, A., GAAZ, T.S., KADHUM, A.A.H., MOHAMED, A.B., 2018. Experimental and theoretical studies of Schiff bases as corrosion inhibitors. Chem Cent J 12. https://doi.org/10.1186/s13065-018-0376-7

KAABI, I., DOUADI, T., DAOUD, D., ISSADI, S., SIBOUS, L., CHAFAA, S., 2021. Synthesis, characterization and anti-corrosion properties of two new Schiff bases derived from diamino diphenyl ether on carbon steel X48 in 1M HCl. J Adhes Sci Technol 35, 559–589. https://doi.org/10.1080/01694243.2020.1816777

KAMEL, M.M., RASHWAN, S.M., MAHMOUD, M.A.A., El-MEKAWY, S.A.A., AWAD, M.K., IBRAHIM, H.E., 2022. Resorcinol Derivative as an Environmentally Friendly Low Carbon Steel Inhibitor in HCl Medium. ACS Omega 7, 17609–17619. https://doi.org/10.1021/acsomega.2c00153

KIRKLAND, N.T., BIRBILIS, N., STAIGER, M.P., 2012. Assessing the Corrosion of Biodegradable Magnesium Implants: A Critical Review of Current Methodologies and Their Limitations. Acta Biomater, 8, 925–936.

KIRKPATRICK, S., GELATT, C.D., VECCHI, M.P., 1983. Optimization by Simulated Annealing.

KUMARI, P., LAVANYA, M., 2021. Optimization of Inhibition Efficiency of a Schiff Base on Mild Steel in Acid Medium: Electrochemical and RSM Approach. J Bio Tribocorros 7. https://doi.org/1-0.1007/s40735-021-00542-3.

MAN, C., DONG, C., WANG, L., KONG, D., LI, X., 2020. Long-Term Corrosion Kinetics and Mechanism of Magnesium Alloy AZ31 Exposed to a Dry Tropical Desert Environment. Corros. Sci. 164, 108274.

MARTINEZ, S., 2002. Inhibitory mechanism of mimosa tannin using molecular modelling and substitutional adsorption isotherms, Materials Chemistry and Physics.

MURALIDHARAN, S., PHANI, ~ K L N, PITCHUMANI, ~ S, RAVICHANDRAN, S., LYER, S.V.K., n.d. Polyamino-Benzoquinone Polymers: A New Class of Corrosion Inhibitors for Mild Steel.

NABATIPOUR, S., MOHAMMADI, S., MOHAMMADI, A., 2020. Synthesis and comparison of two chromone based Schiff bases containing methoxy and acetamido substitutes as highly sustainable corrosion inhibitors for steel in hydrochloric acid. J Mol Struct 1217. https://doi.org/10.1016/j.molstruc.2020.128367.

NATASH MARY, R., NAZARRETH, R., SUCHETAN, P.A., POTLA, K., 2022. Schiff Bases Derived from Triazoles as Corrosion Inhibitors for Maraging Steel in Acid Mixtures: Experimental and Theoretical Studies. Polycycl Aromat Compd 1–22. https://doi.org/10.1080/10406638.2022.2055582

NAZIR, U., AKHTER, Z., JANGUA, N.K., ADEEL ASGHAR, M., KANWAL, S., BUTT, T.M., SANI, A., LIAQAT, F., HUSSAIN, R., SHAH, F.U., 2020. Biferrocenyl Schiff bases as efficient corrosion inhibitors for an aluminium alloy in HCl solution: A combined experimental and theoretical study. RSC Adv 10, 7585–7599. https://doi.org/10.1039/c9ra10692h

OLASUNKANMI, L.O., IDRIS, A.O., ADEWOLE, A.H., WAHAB, O.O., EBENSO, E.E., 2020. Adsorption and Corrosion Inhibition Potentials of Salicylaldehyde-based Schiff Bases of Semicarbazide and p-Toluidine on Mild Steel in Acidic Medium: Experimental and Computational Studies. Surfaces and Interfaces 21. https://doi.org/10.1016/j.surfin.2020.100782

OLASUNKANMI, L.O., OBOT, I.B., EBENSO, E.E., 2016. Adsorption and corrosion inhibition properties of: N -{ n -[1-R-5-(quinoxalin-6-yl)-4,5-dihydropyrazol-3-yl]phenyl}methanesulfonamides on mild steel in 1 M HCl: Experimental and theoretical studies. RSC Adv 6, 86782–86797. https://doi.org/10.1039/c6ra11373g

PADASH, R., RAHIMI-NASRABA, M., SHOKUHI RAD, A., SOBHANI-NASAB, A., JESIONOWSKI, T., EHRLICH, H., 2019. A theoretical study of two novel Schiff bases as inhibitors of carbon steel corrosion in acidic medium. Appl Phys A Mater Sci Process 125. https://doi.org/10.1007/s00339-018-2376-9.

SAADOUNI, M., LAROUJ, M., SALGHI, R., LGAZ, H., JODEH, S., ZOUGAGH, M., SOIZI, A., n.d. Corrosion control of carbon steel in hydrochloric acid by Sulfaguandine: Weight loss, electrochemical and theoretical studies.

SADEEK, S.A., El FARRARGY, A.F., ABD EL RAOUF, M., NEGM, N.A., 2018. Gemini Cationic Schiff Bases and Their Metal Complexes in Preventing Carbon Steel Dissolution in Acidic Medium. Surface Engineering and Applied Electrochemistry 54, 307–318. https://doi.org/10.3103/S1068375518030110.

Saha, S.K., Dutta, A., Ghosh, P., Sukul, D., Banerjee, P., 2016. Novel Schiff-base molecules as efficient corrosion inhibitors for mild steel surface in 1 M HCl medium: Experimental and theoretical approach. Physical Chemistry Chemical Physics 18, 17898–17911. https://doi.org/10.1039/c6cp01993e

SAHA, S.K., MURMU, M., MURMU, N.C., BANERJEE, P., 2021. Synthesis, characterization and theoretical exploration of pyrene based Schiff base molecules as corrosion inhibitor. J Mol Struct 1245. https://doi.org/10.1016/j.molstruc.2021.131098

SHAHABI, S., HAMIDI, S., GHASEMI, J.B., NOROUZI, P., SHAKERI, A., 2019. Synthesis, experimental, quantum chemical and molecular dynamics study of carbon steel corrosion inhibition effect of two Schiff bases in HCl solution. J Mol Liq 285, 626–639. https://doi.org/10.1016/j.molliq.2019.04.137.

SINGH, A.K., QURAISHI, M.A., 2012. Study of Some Bidentate Schiff Bases of Isatin as Corrosion Inhibitors for Mild Steel in Hydrochloric Acid Solution, Int. J. Electrochem. Sci.

SRIVASAVA, V., HAQUE, J., VERMA, C., SINGH, P., LGAZ, H., SALGHI, R., QURAISHI , M.A., 2017. Amino acid based imidazolium zwitterions as novel and green corrosion inhibitors for mild steel: Experimental, DFT and MD studies. J Mol Liq 244, 340–352. https://doi.org/10.1016/j.molliq.2017.08.049

WANG, X., 2021. Study on the Corrosion Inhibition Performance of a Schiff Base for Carbon Steel in 1 M HCl Solution. Int J Electrochem Sci ArticleID:210916. https://doi.org/10.20964/2021.09.36

Zhang, Q.H., Hou, B.S., Xu, N., Xiong, W., Liu, H.F., Zhang, G.A., 2019. Effective inhibition on the corrosion of X65 carbon steel in the oilfield produced water by two Schiff bases. J Mol Liq 285, 223–236. https://doi.org/10.1016/j.molliq.2019.04.072ALEK SEYENKO, O.V., Y.-B. CHAN, M. DE LA PAZ FERNANDEZ, T. BÜLOW, M.J. PANKRATZ, AND E.A. KRAVITZ. 2014. Single serotonergic neurons that modulate aggression in *Drosophila*. Current Biology 24: 2700-2707.

ALI, Y.O., W. ESCALA, K. RUAN, AND R.G. ZHAI. 2011. Assaying locomotor, learning, and memory deficits in *Drosophila* models of neurodegeneration. Journal of Visualized Experiments 49: e2504.

ALTMANN, G. 1959. Der Einfluß statischer elektrischer Felder auf den Stoffwechsel der Insekten. Zeitschrift für Bienenforschung 4: 199-201.

ANDRETIC, R., B. VAN SWINDEREN, AND R.J. GREENSPAN. 2005. Dopaminergic modulation of arousal in *Drosophila*. Current Biology 15: 1165-1175.

ARCH, M., M., VIDAL, R., KOIFFMAN, S.T., MELKIE, AND P.J. CARDONA. 2022. *Drosophila melanogaster* as a model to study innate immune memory. Frontiers in Microbiology, 13, 991678.

ASHBURNER, M., AND C. M. BERGMAN. 2005. *Drosophila melanogaster*: a case study of a model genomic sequence and its consequences. Genome Research. 15: 1661-1667.

BANU, A., S.B. GOWDA, S. SALIM, AND F.

MOHAMMAD. 2023. Serotonergic control of feeding microstructure in *Drosophila*. Frontiers in Behavioral Neuroscience 16:1105579.

BECNEL, J., O. JOHNSON, J. LUO, D.R. NÄSSEL, AND C.D. NICHOLS. 2011. The serotonin 5-HT7Dro receptor is expressed in the brain of *Drosophila*, and is essential for normal courtship and mating. PLoS One **6**: e20800.

BIER, E. 2005. *Drosophila*, the golden bug, emerges as a tool for human genetics. Nature Reviews Genetics 6: 9-23.

BINDOKAS, V.P., J.R. GAUGER, AND B. GREENBERG. 1989. Laboratory investigations of the electrical characteristics of honey bees and their exposure to intense electric fields. Bioelectromagnetics 10: 1-12.

CHANG, H., A. GRYGORUK, E. BROOKS, L. ACKERSON, N. MAIDMENT, R. BAINTON, AND D. KRANTZ. 2006. Overexpression of the *Drosophila* vesicular monoamine transporter increases motor activity and courtship but decreases the behavioral response to cocaine. Molecular Psychiatry 11: 99-113.

CHEN, S., A.Y. LEE, N.M. BOWENS, R. HUBER, AND E.A. KRAVITZ. 2002. Fighting fruit flies: a model system for the study of aggression. Proceedings of the National Academy of Sciences 99: 5664-5668.

COX, M., C. BASSI, M. SAUNDERS, R. NECHANITZKY, I. MORGADO-PALACIN, C. ZHENG, AND T. MAK. 2020. Beyond neurotransmission: acetylcholine in immunity and inflammation. Journal of Internal Medicine 287: 120-133.

DIEGELMANN, S., A. JANSEN, S. JOIS, K. KASTENHOLZ, L.V. ESCARCENA, N. STRUDTHOFF, AND H. SCHOLZ. 2017. The capillary feeder assay measures food intake in *Drosophila melanogaster*. Journal of Visualized Experiments 121: e55024.

EDWARDS, D. 1961. Influence of electrical field on pupation and oviposition in *Nepytia phantasmaria* Stkr. (Lepidoptera: Geometridae). Nature 191: 976-976.

FERNANDEZ, M.P., S. TRANNOY, AND S.J. CERTEL. 2022. Fighting flies: Quantifying and analyzing *Drosophila* aggression. CSH Protocols/*Drosophila* Neurobiology 2022(9): 1-15.

FRENCH, A.S., K.L. SIMCOCK, D. ROLKE, S.E. GARTSIDE, W. BLENAU, AND G.A. WRIGHT. 2014. The role of serotonin in feeding and gut contractions in the honeybee. Journal of Insect Physiology 61: 8-15.

GIORDANI, G., G. CATTABRIGA, A. BECCHI-MANZI, I. DI LELIO, G. DE LEVA, S. GIGLIOTTI, F. PENNACCHIO, G. GARGIULO, AND V. CAVALIERE. 2023. Role of neuronal and non-neuronal acetylcholine signaling in *Drosophila* humoral immunity. Insect Biochemistry and Molecular Biology 153: 103899.

GREENBERG, B., V.P. BINDOKAS, AND J.R. GAUGER. 1981. Biological effects of a 765-kV transmission line: Exposures and thresholds in honeybee colonies. Bioelectromagnetics 2: 315-328.

GREENSPAN, R.J., AND J.-F. FERVEUR. 2000. Courtship in *Drosophila*. Annual review of genetics 34: 205-232.

HARNISH, J.M., N. LINK, AND S. YAMAMOTO. 2021. *Drosophila* as a model for infectious diseases. International journal of molecular sciences 22: 2724.

HASSANEEN, E. 2015. Effect of yellow white mutation on the circadian locomotor activity of the fruit fly *Drosophila melanogaster*: A comparison to Canton S wild-type. Catrina: The International Journal of Environmental Sciences 13: 45-52.

HE, J., Z. CAO, J. YANG, H.-Y. ZHAO, AND W.-D. PAN. 2016. Effects of static electric fields on growth and development of wheat aphid *Sitobion aveanae* (Hemiptera: Aphididae) through multiple generations. Electromagnetic Biology and Medicine 35: 1-7.

JACKSON, C.W., E. HUNT, S. SHARKH, AND P.L. NEWLAND. 2011. Static electric fields modify the locomotory behaviour of cockroaches. Journal of Experimental Biology 214: 2020-2026.

JOHNSON, O., J. BECNEL, AND C.D. NICHOLS. 2009. Serotonin 5-HT2 and 5-HT1A-like receptors differentially modulate aggressive behaviors in *Drosophila melanogaster*. Neuroscience 158: 1292-1300.

KAMEL, M., FOUDA, A. A., RASHWAN, S., MAREI, O. 2022. Burghul Plant Extract as a Green Corrosion Inhibitor for Carbon Steel in Hydrochloric Acid Solution. *Catrina: The International Journal of Environmental Sciences*, 26(1): 19-31. doi: 10.21608/cat.2022.277040

KIM, Y.-C., H.-G. LEE, AND K.-A. HAN. 2007. D1 dopamine receptor dDA1 is required in the mushroom body neurons for aversive and appetitive learning in *Drosophila*. Journal of Neuroscience 27: 7640-7647.

KUME, K., S. KUME, S.K. PARK, J. HIRSH, AND F.R. JACKSON. 2005. Dopamine is a regulator of arousal in the fruit fly. Journal of Neuroscience 25: 7377-7384.

LEGROS, J., G. TANG, J. GAUTRAIS, M.P. FERNANDEZ, AND S. TRANNOY. 2021. Long-term dietary restriction leads to development of alternative fighting strategies. Frontiers in Behavioral Neuroscience 14: 599676.

LEVENGOOD, W., AND M. SHINKLE. 1960. Environmental factors influencing progeny yields in *Drosophila*. Science 132: 34-35.

LEVITT, B.B., H.C. LAI, AND A.M. MANVILLE. 2022. Effects of non-ionizing electromagnetic fields on flora and fauna, part 2 impacts: how species interact with natural and man-made EMF. Reviews on Environmental Health 37: 327-406.

MASEK, P., K. WORDEN, Y. ASO, G. M. RUBIN, AND A. C. KEENE. 2015. A dopamine-modulated

neural circuit regulating aversive taste memory in *Drosophila*. Current biology 25: 1535-1541.

MATSUDA, Y., T. NONOMURA, K. KAKUTANI, Y. TAKIKAWA, J. KIMBARA, Y. KASAISHI, K. OSAMURA, S.-I. KUSAKARI, AND H. TOY-ODA. 2011. A newly devised electric field screen for avoidance and capture of cigarette beetles and vinegar flies. Crop Protection 30: 155-162.

MAW, M. 1961. Behavior of an insect on an electrically charged surface. *The Canadian Entomologist* 93: 391-393.

MIRZOYAN, Z., M. SOLLAZZO, M. ALLOCCA, A.M. VALENZA, D. GRIFONI, AND P. BELL-OSTA. 2019. *Drosophila melanogaster*: A model organism to study cancer. Frontiers in genetics 10: 51.

MONASTIRIOTI, M. 1999. Biogenic amine systems in the fruit fly *Drosophila melanogaster*. Micros-copy Research and Technique 45: 106-121.

NECKAMEYER, W.S. 1998. Dopamine modulates female sexual receptivity in *Drosophila melano-gaster*. Journal of Neurogenetics 12: 101-114.

NEWLAND, P.L., M.S. AL GHAMDI, S. SHARKH, H. AONUMA, AND C.W. JACKSON. 2015. Exposure to static electric fields leads to changes in biogenic amine levels in the brains of *Drosophila*. Proceedings of the Royal Society B: Biological Sciences 282: 20151198.

NEWLAND, P.L., E. HUNT, S.M. SHARKH, N. HAMA, M. TAKAHATA, AND C.W. JACKSON. 2008. Static electric field detection and behavioural avoidance in cockroaches. Journal of Experimental Biology 211: 3682-3690.

NICHOLS, C.D., J. BECNEL, AND U.B. PANDEY. 2012. Methods to assay *Drosophila* behavior. Journal of Visualized Experiments 61: e3795.

PALL, M.L. 2013. Electromagnetic fields act via activation of voltage-gated calcium channels to produce beneficial or adverse effects. Journal of Cellular and Molecular Medicine 17: 958-965.

PANAGOPOULOS, D. 2015. Pulsed electric field increases reproduction. International Journal of Radiation Biology 92: 94-106.

PERUMPRAL, J.V., U. EARP, AND J. STANLEY. 1978. Effects of electrostatic field on locational preference of house flies and flight activities of cabbage loopers. Environmental Entomology 7: 482-486.

PETRI, A.-K., K. SCHMIEDCHEN, D. STUNDER, D. DECHENT, T. KRAUS, W.H. BAILEY, AND S. DRIESSEN. 2017. Biological effects of exposure to static electric fields in humans and vertebrates: a systematic review. Environmental Health 16: 1-23.

PICCIOTTO, M.R., M.J. HIGLEY, AND Y.S. MINEUR. 2012. Acetylcholine as a neuromodulator: cholinergic signaling shapes nervous system function and behavior. Neuron 76: 116-129.

PIZZO, A.B., C.S. KARAM, Y. ZHANG, H. YANO, R.J. FREYBERG, D.S. KARAM, Z. FREYBERG, A. YAMAMOTO, B.D. MCCABE, AND J.A. JAVITCH. 2013. The membrane raft protein Flotillin-1 is essential in dopamine neurons for amphetamine-induced behavior in *Drosophila*. Molecular Psychiatry 18: 824-833.

POORYASIN, A., AND A. FIALA. 2015. Identified serotonin-releasing neurons induce behavioral quiescence and suppress mating in *Drosophila*. Journal of Neuroscience 35: 12792-12812.

REDLARSKI, G., B. LEWCZUK, A. ŻAK, A. KONCICKI, M. KRAWCZUK, J. PIECHOCKI, K. JAKUBIUK, P. TOJZA, J. JAWORSKI, AND D. AMBROZIAK. 2015. The influence of electromagnetic pollution on living organisms: historical trends and forecasting changes. BioMed Research International 2015.

SAHU, S., G. DHAR, AND M. MISHRA. 2020. Methods to detect the complex behaviours in *Drosophila*. In Mishra, M. (eds) Fundamental Approaches to Screen Abnormalities in *Drosophila*. Springer Protocols Handbooks. Springer, New York, USA.

SCHMIEDCHEN, K., A.-K. PETRI, S. DRIESSEN, AND W.H. BAILEY. 2018. Systematic review of biological effects of exposure to static electric fields. Part II: Invertebrates and plants. Environmental Research 160: 60-76.

SCHNEIDER, C.A., W.S. RASBAND, AND K.W. ELICEIRI. 2012. NIH Image to ImageJ: 25 years of image analysis. Nature Methods 9: 671-675.

SCHROLL, C., T. RIEMENSPERGER, D. BUCHER, J. EHMER, T. VÖLLER, K. ERBGUTH, B. GERBER, T. HENDEL, G. NAGEL, AND E. BUCHNER. 2006. Light-induced activation of distinct modulatory neurons triggers appetitive or aversive learning in *Drosophila* larvae. Current Biology 16: 1741-1747.

SCHWAERZEL, M., M. MONASTIRIOTI, H. SCHOLZ, F. FRIGGI-GRELIN, S. BIRMAN, AND M. HEISENBERG. 2003. Dopamine and octopamine differentiate between aversive and appetitive olfactory memories in *Drosophila*. Journal of Neuroscience 23: 10495-10502.

SHEPHERD, S., G. HOLLANDS, V.C. GODLEY, S.M. SHARKH, C.W. JACKSON, AND P.L. NEWLAND. 2019. Increased aggression and reduced aversive learning in honey bees exposed to extremely low frequency electromagnetic fields. PLoS One 14: e0223614.

SHEPHERD, S., M. LIMA, E. OLIVEIRA, S. SHARKH, C. JACKSON, AND P. NEWLAND. 2018. Extremely low frequency electromagnetic fields impair the cognitive and motor abilities of honey bees. Scientific Reports 8: 1-9.

SHOWELL, S.S., Y. MARTINEZ, S. GONDOLFO, S. BOPPANA, AND H.O. LAWAL. 2020. Overexpression of the vesicular acetylcholine transporter disrupts cognitive performance and causes age-dependent locomotion decline in *Drosophila*. Molecular and Cellular Neuroscience 105: 103483.

SIMON, A.F., R. DANIELS, R. ROMERO-

CALDERON, A. GRYGORUK, H.-Y. CHANG, R. NAJIBI, D. SHAMOUELIAN, E. SALAZAR, M. SOLOMON, AND L.C. ACKERSON. 2009. *Drosophila* vesicular monoamine transporter mutants can adapt to reduced or eliminated vesicular stores of dopamine and serotonin. Genetics 181: 525-541.

SIMON, J.C., AND U. HEBERLEIN. 2020. Social hierarchy is established and maintained with distinct acts of aggression in male *Drosophila melanogaster*. Journal of Experimental Biology 223: jeb232439.

STEVENSON, P.A., H.A. HOFMANN, K. SCHOCH, AND K. SCHILDBERGER. 2000. The fight and flight responses of crickets depleted of biogenic amines. Journal of Neurobiology 43: 107-120.

SUZUKI, M., K. SANGO, AND Y. NAGAI. 2022. Roles of α-Synuclein and disease-associated factors in *Drosophila* models of Parkinson's disease. International Journal of Molecular Sciences 23: 1519.

THILL, A., M.-C. CAMMAERTS, AND A. BALMORI. 2023. Biological effects of electromagnetic fields on insects: a systematic review and meta-analysis. Reviews on Environmental Health.

TIERNEY, A.J. 2020. Feeding, hunger, satiety and serotonin in invertebrates. Proceedings of the Royal Society B: Biological Sciences 287: 20201386.

TONG, Z., Z. DONG, AND T. ASHTON. 2016. Analysis of electric field influence on buildings under high-voltage transmission lines. IET Science, Measurement & Technology 10: 253-258.

TOURAB, W., AND A. BABOURI. 2016. Measurement and modeling of personal exposure to the electric and magnetic fields in the vicinity of high voltage power lines. Safety and Health at Work **7**: 102-110.

VILLELLA, A., AND J.C. HALL. 2008. Neurogenetics of courtship and mating in *Drosophila*. Advances in Genetics 62: 67-184.

WADDELL, S. 2013. Reinforcement signalling in *Drosophila*; dopamine does it all after all. Current opinion in neurobiology 23: 324-329.

WATSON, D. 1984. Effect of an electric field on insects. New Zealand Journal of Science 27: 139.

WHITE, D., R.P. DE SOUSA ABREU, A. BLAKE, J. MURPHY, S. SHOWELL, T. KITAMOTO, AND H.O. LAWAL. 2020. Deficits in the vesicular acetylcholine transporter alter lifespan and behavior in adult *Drosophila melanogaster*. Neurochemistry International 137: 104744.

WHO. 2007. Extremely low frequency fields. 92415-72388, World Health Organization, Gneva.

WOLFGANG, B., AND B. ARND. 2001. Molecular and pharmacological properties of insect biogenic amine receptors: Lessons from *Drosophila melanogaster* and *Apis mellifera*. Archives of Insect Biochemistry and Physiology 48: 13-38.

YAMAMOTO, S., AND E.S. SETO. 2014. Dopamine dynamics and signaling in *Drosophila*: an overview of genes, drugs and behavioral paradigms. Experimental animals 63: 107-119.

ZHANG, S., Y. YIN, H. LU, AND A. GUO. 2008. Increased dopaminergic signaling impairs aversive olfactory memory retention in *Drosophila*. Biochemical and Biophysical Research Communications 370: 82-86.

.

تقييم قاعدة شيف السالين كمثبط لتآكل الصلب منخفض الكربون فى وسط حمض الهيدروكلوريك: دراسات عملية وحاسوبية

أمل رفعت[1] ، مدحت كامل[1]، أحمد أبوالمجد[1]، صلاح رشوان[1]،عبد العزيز فوده[2] ،محمد عواد [3]،فاتن أتلام[3]

[1] كلية العلوم-قسم الكيمياء-جامعة قناة السويس-الاسماعيلية- مصر

[2] كلية العلوم- قسم الكيمياء-جامعة المنصورة- المنصورة- مصر

[3] كلية العلوم- قسم الكيمياء-جامعة طنطا-طنطا- مصر

الملخص العربي

في هذه الدراسة تم تحضير وتقييم الأداء المثبط لمركب N، N′-bis (الساليسيليدين) الإيثيلين-1،2-ديامين (قاعدة شيف السالين) لتآكل الصلب منخفض الكربون في محلول حامض الهيدروكلوريك ذو التركيز النصف مولاري، من خلال طريقة الفقد في الوزن (WL) وتقنيتي مطيافية المعاوقة الكهروكيميائية (EIS) والاستقطاب الديناميكى الفعال (PP). تم تحضير مركب قاعدة شيف السالين وتم اثبات تركيبه عن طريق تقنيتي بروتون الرنين المغناطيسى والأشعة تحت الحمراء. ولقد أوضحت النتائج العملية زيادة كفاءة التثبيط مع زيادة تركيز قاعدة شيف السالين. عند تركيز 300 جزء من المليون من المركب المحضر كانت كفاءة التثبيط 75.4% وذلك عند 298 درجة مطلقة، بينما انخفضت كفاءة التثبيط إلى 69.5 % عندما زادت درجة الحرارة من 298 إلى 333 درجة مطلقة. وجود المركب المحضر في بيئة التآكل قلل من سعة الطبقة المزدوجة. وكثافة تيار التآكل (icorr) بسبب تكوين طبقة واقية منه على سطح الصلب الكربوني. هذا، ولقد أظهرت النتائج أن المركب المحضر ينتمي للنوع الخليط حيث أنه يثبط كلاً من التفاعل الأنودي والكاثودي على السواء. كما أكدت النتائج أن ادمصاص المركب المحضر يتبع نموذج العالم لانجمير. أكدت نتائج فحص سطح الصلب الكربوني باستخدام المسح بالميكرسكوب الالكتروني والأشعة السينية المشتتة للطاقة وجود طبقة مدمصة رقيقة من المركب المحضر على سطح الصلب الكربوني، والتي تعزله عن بيئة التآكل. تم استخدام نظرية الكثافة الوظيفية (DFT) ومحاكاة مونت كارلو (MC) لتوضيح كيفية اتصال وشكل جزئيات قاعدة شيف السالين مع / على الصلب الكربوني . أشارت النتائج أن مركب قاعدة شيف السالين يرتبط بسطح الصلب الكربوني من خلال زوج الإلكترونات الحر الموجود على ذرتي الأكسجين والنيتروجين، بالإضافة إلى إلكترونات باي الخاصة بحلقة البنزين. ولقد تم حساب طاقة الترابط بين المركب المحضر والصلب الكربوني ووجد أنها 160.150 كيلو جول/ مول. ولقد أكدت النتائج الحاسوبية على القدرة التثبيطية لمركب قاعدة شيف السالين لتآكل الصلب الكربوني في بيئة حامض الهيدروكلوريك.